Article

Study on Numerical Simulation of Formation Deformation Laws Induced by Offshore Shallow Gas Blowout

Zhiming Yin [1], Yingwen Ma [1], Xiangqian Yang [1], Xinjiang Yan [1], Zhongying Han [2], Yanbo Liang [2,*] and Penghui Zhang [2]

1 CNOOC Research Institute Co., Ltd., Beijing 100028, China; yinzhm@cnooc.com.cn (Z.Y.); mayw@cnooc.com.cn (Y.M.); yangxq15@cnooc.com.cn (X.Y.); yanxj3@cnooc.com.cn (X.Y.)
2 School of Petroleum Engineering, China University of Petroleum (East China), Qingdao 266580, China; hanzhying@upc.edu.cn (Z.H.); z22020095@s.upc.edu.cn (P.Z.)
* Correspondence: b20020011@s.upc.edu.cn

Abstract: To address the deformation and instability characteristics of a formation after an offshore shallow gas well blowout, a theoretical model of formation deformation caused by shallow gas blowouts was constructed, based on porous elastic medium theory and incorporating the sand-out erosion criterion. The spatiotemporal dynamics of formation subsidence were then investigated, and deformation patterns during a blowout were analyzed under various factors. The results indicate that, following a blowout, a shallow gas formation near a borehole experiences significant subsidence and uplift at the upper and lower ends, with the maximum subsidence values at 12 h, 24 h, 36 h, and 48 h post blowout being 0.072 m, 0.132 m, 0.164 m, and 0.193 m, respectively. The overlying rock layer forms a distinctive "funnel" shape, exhibiting maximum subsidence at the borehole, while more distant strata show uniform subsidence. The effective stress within the shallow gas stratum and surrounding rock layers increases gradually during the blowout, with lesser impact in distant areas. The ejection rate and sand blast volume demonstrate an exponential change pattern, with a rapid decline initially and later stabilization. Formation deformation correlates positively with factors like burial depth; shallow gas layer extent; pressure coefficient; sand blast volume; gas blowout rate; and bottomhole difference pressure. Formation pressure, ejection rate, and bottomhole difference pressure have the most significant impact, followed by sand blast volume and burial depth, while the extent of the shallow gas layer has a less pronounced effect. These simulation results offer valuable theoretical insights for assessing the destabilization of formations due to blowouts.

Keywords: offshore drilling; shallow gas; well blowout; formation deformation and instability; numerical simulation

1. Introduction

Marine oil and gas resources constitute a vital component of the global energy supply, with their development and utilization emerging as a prominent topic in the energy sector in recent years [1,2]. According to the International Energy Agency (IEA), from 2000 to 2016, global marine oil production comprised 29–34% of total oil extraction, while marine natural gas production represented 27–31% [3,4]. As the global energy supply-demand scenario becomes more constrained, the exploitation of marine oil and gas resources assumes significant importance for the security and stability of global energy supply. The offshore oil and gas drilling and extraction process poses various challenges, demanding enhanced stability, safety, and advancement in platform structure and equipment. In addition, the seabed is characterized by complex geological conditions and active tectonic movements, often accompanied by submarine geological disasters caused by submarine landslides; shallow gas; gas hydrates; gas escape pits; and submarine steep hurdles, which pose a serious threat to the safe and efficient exploitation of marine oil and gas [5–7]. Shallow gas usually refers to organic gas gathered in the shallow stratum below a 1000 m seafloor, which

usually does not have mining value, and the composition is mostly dominated by methane, which can be subdivided into biogenic methane, shallow gas, and pyrogenic methane shallow gas, according to its different genesis [8–10]. After shallow gas forms, it is prone to accumulate in high-permeability sandy soil layers, and when covered by low-permeability silt-like soil, it forms a high-pressure gas pocket. When drilling operations encounter shallow gas layers, complex situations such as wellbore gas invasion; well kick; wellbore collapse; and wellbore instability may occur, which can lead to major accidents such as blowout and fire, and even platform collapse in severe cases [11–13]. The fundamental reason for shallow gas well blowout accidents is that the pressure of the wellbore fluid column cannot balance the pressure of the shallow gas layer [14–17]. Blowouts not only pose threats to on-site personnel and equipment, but can also cause varying degrees of damage to the soil around the wellbore. If natural gas escapes and encounters sparks, combustion can occur, making it extremely hazardous. A common emergency response method is to inject high-density barite mud into the well to increase pressure and halt the ongoing blowout [18–20].

Numerous scholars have conducted research on the identification, evaluation, and control of shallow gas blowouts, through field tests, theoretical analysis, and numerical simulation methods. Field tests consume a significant amount of manpower and resources and pose certain risks [21–24]. Theoretical analysis includes various empirical models, such as fault tree analysis, event tree analysis, fuzzy mathematics, and the analytic hierarchy process [25–28]. However, these evaluation methods are primarily suited for conventional drilling operations, and have limitations with lower accuracy when applied to complex offshore operations. In terms of numerical simulation, computational fluid dynamics (CFD) methods are widely employed for the assessment of blowout incidents. Dadashzadeh et al. exploited the FDS CFDs code, and modelled hydrogen release and dispersion with different ventilation conditions [29]. Ma et al. used the Fluent software to investigate sour gas dispersion. They found that some numerical and physical parameters, such as mesh size and leakage source style, have a significant impact on simulation accuracy [30]. Li et al. utilized a 3D CFD-based approach to study the evolution of offshore blowout accidents, integrating gas release, dispersion, and deflagration while assessing their impact on offshore platforms [31]. They also discussed the corresponding prevention and mitigation strategies based on simulation results [32]. In addition to CFD methods, other numerical approaches are used for the assessment of blowout incidents, such as the discrete element method (DEM), and the finite element method (FEM). Based on gas–water two-phase flow theory, Lei et al. established a numerical model to calculate gas invasion volume to quantify the shallow gas risk during deepwater drilling [33]. Cheng et al. proposed a semi-resolved CFD-DEM model to study the gas release and fine particle migration within gap-graded soils [34]. While these approaches help study gas diffusion and combustion behavior, some models are criticized for being overly simplified and relying on numerous assumptions.

Existing research on shallow gas well blowouts mainly centers on predicting flow rates, assessing risks, studying wellhead smoke flow, and evaluating post-fire platform stability. The substantial mud and sediment movement during blowouts deplete formations, causing wellbore vulnerability to collapse and stress concentration. This leads to overall geological deformation, impacting offshore drilling. A comprehensive understanding of post-blowout deformation and key factors influencing formation stability is crucial. In this paper, an innovative theoretical model is proposed, integrating porous elastic media theory and sand erosion criteria, to analyze post-blowout geological formation settlement. This unique approach promises valuable insights into formation instability following blowouts, enhancing our ability to assess and manage risks in such scenarios.

2. Theoretical Model for Formation Deformation

2.1. Model Assumptions

As shown in Figure 1, during a blowout, the shallow gas formation undergoes elastic deformation initially, influenced by a significant pressure gradient in the shallow gas layer.

Upon surpassing the elastic deformation limit, the formation transitions into the plastic deformation stage. Once the plastic deformation reaches the critical threshold for equivalent plastic deformation, continuous ejection of mud and sediment from the formation ensues. Given the rapid nature of blowout occurrences, this study simplifies the consideration of elastic-plastic changes in the formation. Furthermore, the theoretical model in this paper operates under the following assumptions:

(1) The sand layer is only subjected to vertical pressure from the overlying rock strata, neglecting lateral pressures caused by tectonic movements, etc.
(2) The blowout formation experiences continuous sand ejection, with the rock framework considered as a uniformly isotropic porous elastic medium.
(3) The flow of sand and gas occurs at the same velocity, and the flow of the sand–gas mixture follows Darcy's law and is treated as an isothermal process.
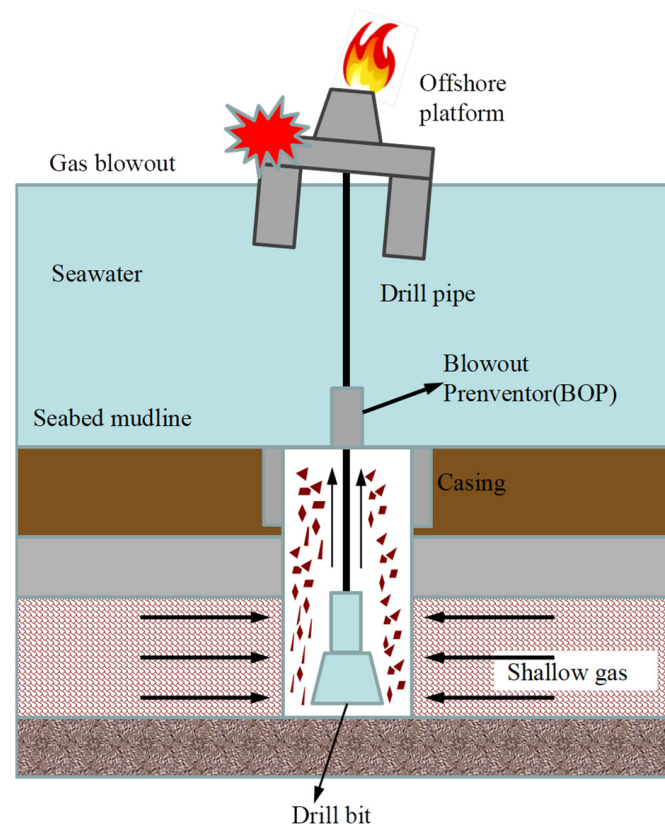

Figure 1. Schematic diagram of shallow gas layer blowout.

2.2. Seepage Field Model

Analyzing a small element taken from the geological formation, assuming that the fluid in the shallow gas formation is a single-phase fluid (gas phase), the small element contains gas, fluidized solids (flowing sand), and a rock framework. Assuming continuous sand ejection from the formation and considering the rock framework as a continuous medium, the gas phase, flowing sand, and rock framework satisfy the following continuity equations:

$$\frac{\partial[\rho_g(1-C)\phi]}{\partial t} + \nabla \cdot (\rho_g(1-C)\phi v_g) = 0 \tag{1}$$

$$\frac{\partial[\rho_s C\phi]}{\partial t} + \nabla \cdot (\rho_s C\phi v_{fs}) = m \tag{2}$$

$$\frac{\partial[\rho_s(1-\phi)]}{\partial t} + \nabla \cdot (\rho_s(1-\phi)v_s) = -m \tag{3}$$

where subscripts g, fs, s represent gas, flowing sand, and the geological formation skeleton, respectively. Formation density, kg/m^3, is ρ; t is erosion time, s; ϕ is porosity; v_s is gas flow velocity, m/s; and C is the sand content in the pore space.

Considering the density of the formation skeleton to be constant, $\rho_s = $ const, and its velocity $v_s = 0$, substituting it into Formula (3) yields as follow:

$$\frac{\partial \phi}{\partial t} = \frac{m}{\rho_s} \tag{4}$$

According to the erosion criterion proposed by Papamichos [35,36], the erosion rate of the rock framework per unit time can be expressed as follows:

$$m = \rho_s \lambda (1 - \phi) v_s \tag{5}$$

where λ is the erosion coefficient, m^{-1}.

The flow of shallow gas follows the ideal gas state equation:

$$\rho_g = \frac{M_g}{RT} p \tag{6}$$

where M_g is the molar mass of the gas, kg/mol; R is the ideal gas constant; and T is the temperature, K. The flow velocity and pressure of shallow gas at the seabed follow Darcy's law.

$$v = -\frac{k_g}{\mu} \nabla p \tag{7}$$

where μ is the gas dynamic viscosity coefficient, Pa·s; and k_g is the permeability of the shallow gas formation, m².

2.3. Deformation Field Equations

The stress field equations mainly include equilibrium equations, physical equations, and geometric equations. Neglecting the effect of inertial forces, the equilibrium equation for shale reservoir deformation can be expressed as follows:

$$\sigma_{ij,j} + f_i = 0 \tag{8}$$

where σ_{ij} is the stress component, Pa; and f_i is the volumetric force component, Pa.

The geometric equation is given by

$$\varepsilon_{ij} = \frac{1}{2} \left(u_{i,j} + u_{j,i} \right) \tag{9}$$

where ε_{ij} is the total strain component; and u_i is the displacement component, m.

The constitutive equation for porous elastic media can be expressed as follows:

$$\varepsilon_{ij} = \frac{1}{2G} \sigma_{ij} - \left(\frac{1}{6G} - \frac{1}{9K} \right) \sigma_{kk} \delta_{ij} + \frac{\alpha}{3K} p \delta_{ij} \tag{10}$$

where $G = E/2(1+v)$, $K = E/3(1-2v)$, $\sigma_{kk} = \sigma_{11} + \sigma_{22} + \sigma_{33}$; G is shear modulus; K is bulk modulus; E is Young's modulus; v is Poisson's ratio; α is the Biot coefficient; and δ_{ij} is Kronecker delta. From Equations (8)–(10), the governing equation for the stress field can be derived as follows:

$$G u_{i,kk} + \frac{G}{1-2v} u_{k,ki} - \alpha p_{,i} + f_i = 0 \tag{11}$$

2.4. State Equations

By substituting Formula (5) into Formula (4), the dynamic change equation of porosity in the shallow gas formation can be obtained as follows:

$$\frac{\partial \phi}{1-\phi} = \lambda v_{\mathrm{g}} \partial \mathrm{t} \tag{12}$$

Separating variables in the above equation:

$$\ln(1-\phi) = e^{\lambda v_g t + C_1} \tag{13}$$

By substituting the initial conditions $\phi = \phi_0$, $t = t_0$ into the Equation (13), the dynamic evolution equation of porosity in the shallow gas formation during the blowout process can be obtained as follows:

$$\phi = 1 - (1-\phi_0)e^{-\lambda v_g t} \tag{14}$$

Assuming that the porosity ϕ and permeability k_{g} of the shallow gas formation satisfy the Kozeny–Carman model [37–39], the dynamic evolution equation for permeability can be expressed as follows:

$$k_{\mathrm{g}} = k_0 \left(\frac{\phi}{\phi_0}\right)^3 \left(\frac{1-\phi_0}{1-\phi}\right)^2 \tag{15}$$

During the blowout process, the ejection of gas carrying a large amount of mud and sand increases the porosity, weakening the formation strength. In the porous elastic constitutive model used in this paper, the decrease in bearing capacity is mainly reflected in the change of the elastic modulus model. The dynamic evolution equation for elasticity is expressed as follows:

$$E = (1 - 4.875\phi) \times 10^9 \tag{16}$$

3. Numerical Model

3.1. Base Case Model

To study the spatiotemporal evolution of strata deformation during blowout events, we initially established a fundamental numerical model for this research. Considering the symmetry of the strata, this foundational model was a two-dimensional axisymmetric plane model as shown in Figure 2. The model included overlying rock layers, underlying rock layers, a shallow gas layer, and other interlayers. In Figure 3, the overall dimensions of the model were 300 m (length) × 1200 m (width), with the shallow gas layer buried at a depth of 600 m, having a thickness of 60 m and a length of 100 m. The mud line was located at a depth of 50 m on the seabed, and seawater pressure was applied to the top boundary of the model in the form of a uniformly distributed load, with a value of 0.5 Mpa. The bottom displacement was fixed, and the normal displacement was fixed on the left and right boundaries. To obtain more precise numerical solutions, the grid was locally refined in the area near the shallow gas layer and close to the wellbore, resulting in a total of 16,542 grids within the model. The shallow gas layer was assigned a high-pressure coefficient to simulate its high-pressure characteristics. The high-pressure coefficient was the ratio of formation pressure to static liquid column pressure, and the pressure coefficient of abnormally high-pressure formations was usually 1.2–2.0. During the blowout process, a fixed pressure or flow boundary was applied to the shallow gas layer near the wellbore boundary. For convenience in the study, as shown in Figure 3, displacement measurement lines l_1, l_2, and l_3 were set up in the overlying rock layers, and seven measurement points, P_1 to P_7, were positioned around the wellbore. The relevant parameters of the basic model are presented in Table 1.
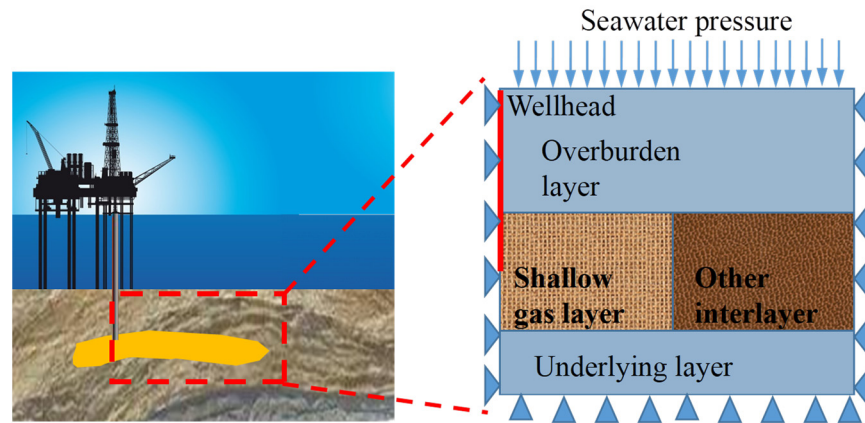
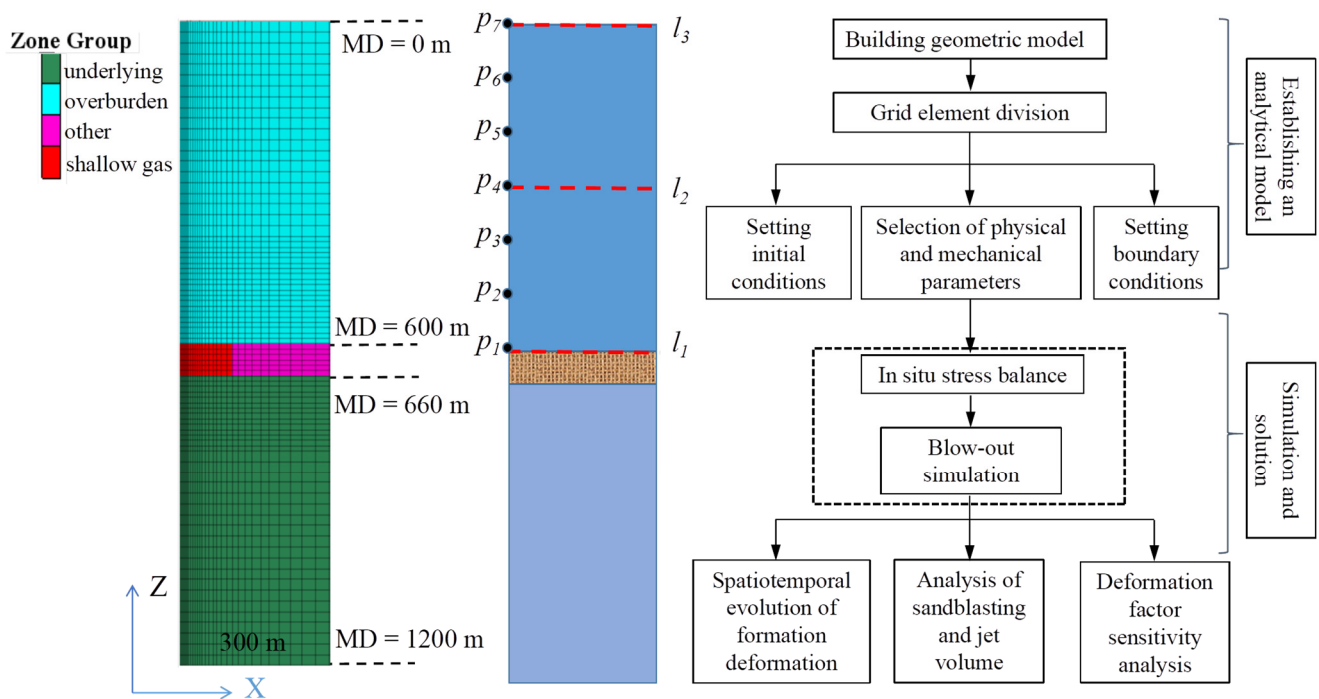**Figure 2.** Schematic diagram of two-dimensional plane model.

Figure 3. Numerical model grid division, layout of measuring lines and points and simulation workflow.

Table 1. Physical and mechanical parameters of the formation in the basic model.

Parameter	Value	Unit
Molar mass of gas M_g	0.016	kg/mol
Ideal gas constant R	8.314	J/(mol·K)
Temperature T	269	K
Erosion coefficient λ	1.5	m^{-1}
Gas dynamic viscosity μ	2.01×10^{-5}	Pa·s
Elastic modulus of shallow gas layer E_g	0.2	GPa
Poisson's ratio v_g	0.25	
Initial porosity of shallow gas layer ϕ_{g0}	0.5	
Initial permeability of shallow gas layer k_{g0}	0.5	D
Density of shallow gas layer ρ_{gs}	1700	kg/m^3
Elastic modulus of overlying layer E_o	2	GPa
Poisson's ratio of overlying layer v_o	0.3	
Initial porosity of overlying layer ϕ_{o0}	0.3	
Initial permeability of overlying layer k_{o0}	0.01	D

Table 1. *Cont.*

Parameter	Value	Unit
Density of overlying layer ρ_o	2000	kg/m^3
Elastic modulus of underlying layer E_u	5	GPa
Poisson's ratio of underlying layer v_u	0.3	
Initial porosity of underlying layer ϕ_{u0}	0.2	
Initial permeability of underlying layer k_{u0}	0.02	D
Density of underlying layer ρ_u	2200	kg/m^3
Seawater depth	20	m
Pressure coefficient of shallow gas layer	1.6	

3.2. Simulation Scheme

Through previous research, it can be found that the main factor causing formation deformation is the decrease in bearing capacity of the formation, while the weakening of formation strength is mainly caused by the ejection of a large amount of mud and sand. Therefore, it is important to study the impact of different pressure differences and sandblasting amounts on formation deformation. In addition, there are other factors that can affect formation deformation, including shallow gas layer burial depth, range, bottom-hole pressure difference, and gas blowout rate. Based on the established numerical model, simulations were conducted for different factors. Two categories of factors were selected: inherent formation factors and operational factors, encompassing six parameters. Each factor was simulated with five different values. The specific factor simulation scheme is detailed in the Table 2. It should be noted that the models of different sandblasting quantities mentioned above correspond to the states after a blowout of 3.5 h, 7.5 h, 13.5 h, 21 h, and 35 h, respectively.

Table 2. Factor analysis simulation scheme.

Factor	Parameter	Lower Value	Base Value	Higher Value
Inherent formation factors	Buried depth/m	400, 500	600	700, 800
	Shallow gas range/m	60, 80	100	120, 140
	Pressure coefficient	1.2, 1.4	1.6	1.8, 2.0
	Sand blasting volume/m^3	300, 600	900	1200, 1500
Operational factors	Pressure difference/MPa	1.26, 2.76	4.26	5.76, 7.26
	Gas blowout rate/m^3/h	0.6×10^5, 0.8×10^5	1×10^5	1.2×10^5, 1.4×10^5

4. Analysis of Simulation Results

4.1. Spatiotemporal Evolution of Formation Settlement during Blowout

Figure 4 provides overall formation deformation cloud diagrams at different times (12 h, 24 h, 36 h, and 48 h) after the blowout. It can be seen that significant settlement and uplift occur at the shallow gas formation's upper and lower ends near the wellbore after the gas blowout. Over time, deformation of rock layers near the shallow gas formation increases. The maximum settlement values at different times are 0.072 m, 0.132 m, 0.164 m, and 0.193 m, respectively. The maximum uplift values are 0.062 m, 0.074 m, 0.084 m, and 0.088 m. The settlement extends from the bottom upwards to the seabed mudline, while the uplift range increases, its degree gradually decreases.
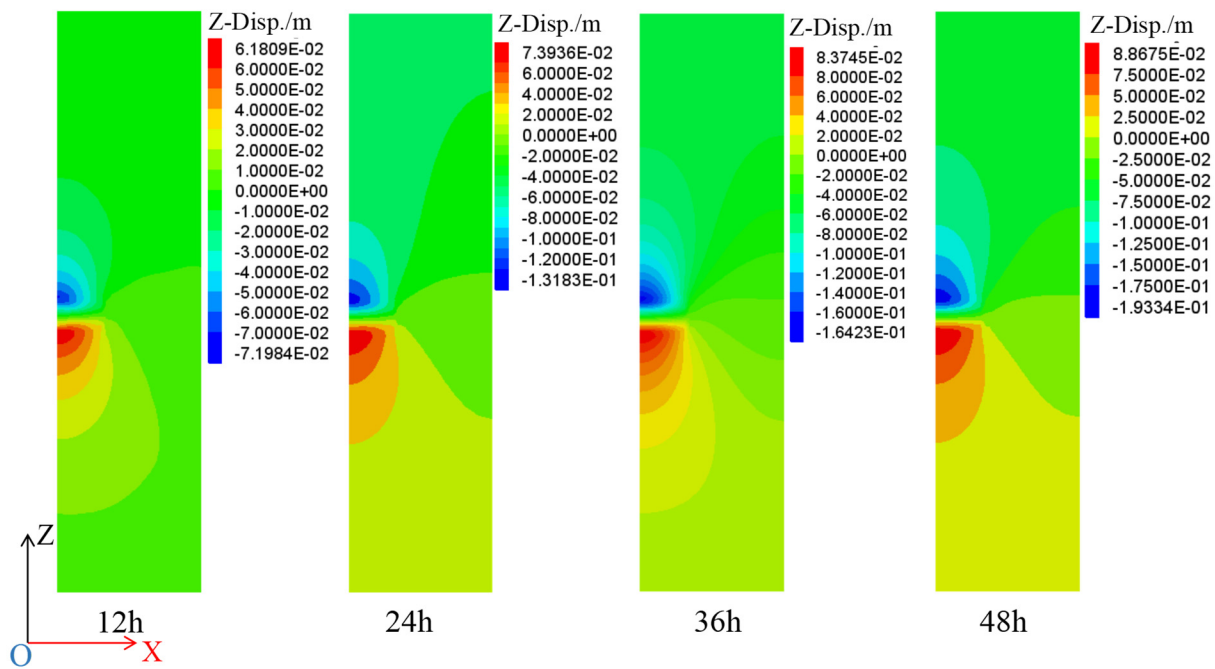
Figure 4. Cloud chart of overall formation deformation at different times during the blowout process.

Analysis of settlement values at different positions above the shallow gas layer was conducted at 0 m, 300 m, and 600 m along the x-axis. It can be seen from Figure 5a that the deformation curves show a distinct "funnel" shape in settlement near the shallow gas layer, with larger settlements closer to the wellbore, and minimal impact on far-field formations. After 12 h of the blowout, distant interlayers show almost no deformation. The maximum settlement values increase over time, but the rate of settlement gradually decreases. As shown in the Figure 5b,c, the upper rock layers above the shallow gas layer experience smaller settlements, especially at 600 m above the layer, showing a uniform downward movement. This is attributed to the significant mud and sand blasting near the wellbore, weakening the formation strength, resulting in a 'cantilever beam' structure at the bottom of the overlying rock layers. The upper formations uniformly descend due to the overall weakening of the lower layers.

Figure 6 presents the wellbore measurement points' settlement values over time, and their final values after 48 h. As seen in Figure 6a, the settlement value at the wellbore measurement points increases with time. The settlement at the measuring point increases continuously over time, and the overall rate of change is relatively uniform. However, there are some fluctuations in human behavior, which are caused by certain fluctuations in the effective stress at the measuring point. Initially, at the outset of the blowout, the settlement rate at measurement point 1 is rapid, showing a sharp decline. In contrast, measurement points 4–7 show almost no settlement within the first 10 h of the blowout. The largest deformation occurs near the wellbore in the vicinity of the shallow gas layer, with the final settlement value reaching 0.189 m. The final settlement values at positions 400–600 m above the shallow gas layer remain relatively constant, approximately around 0.07 m, reaffirming that the upper formations above the shallow gas layer experience less settlement but demonstrate a consistent, uniform downward movement.
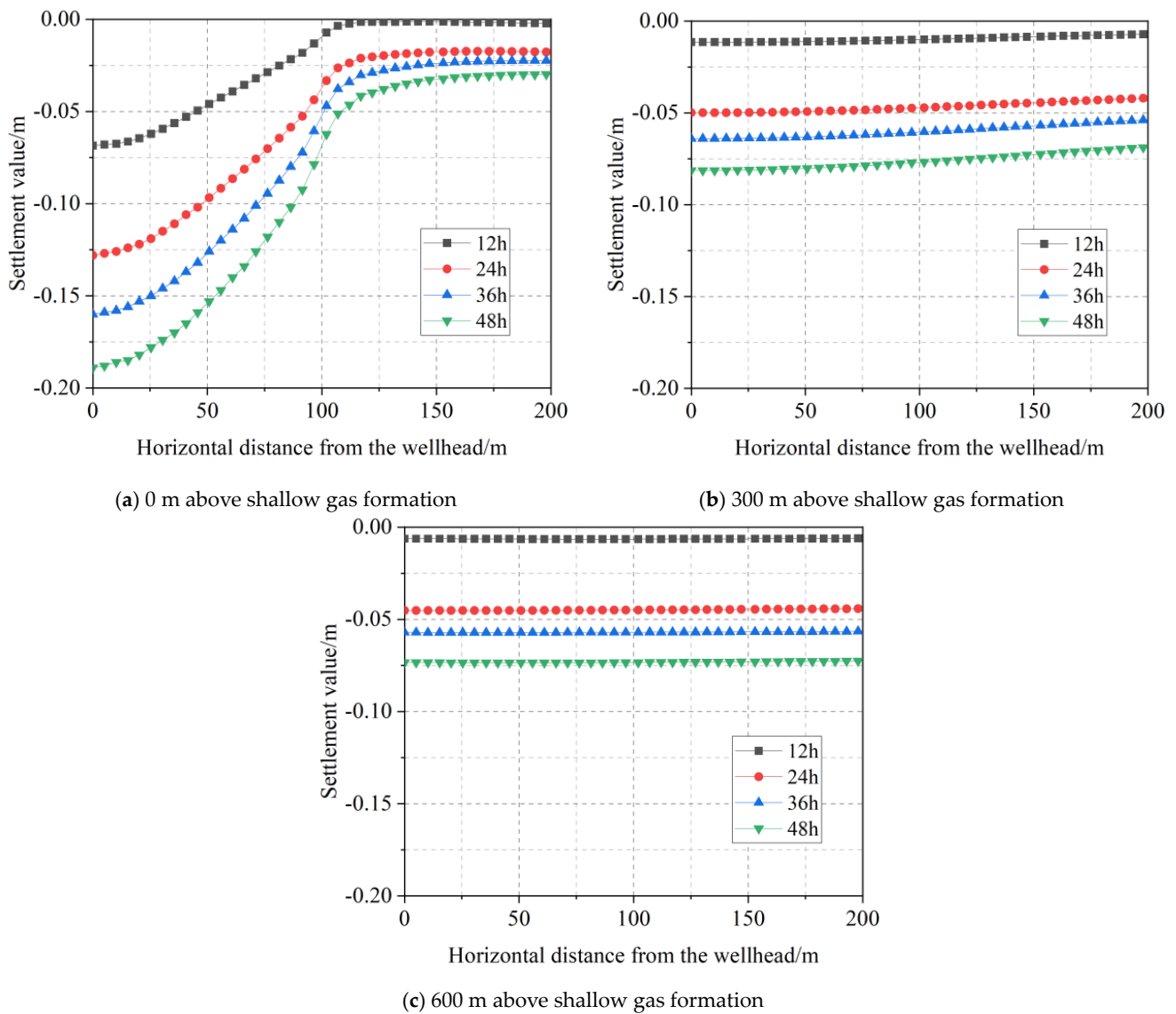
(**a**) 0 m above shallow gas formation　　　　(**b**) 300 m above shallow gas formation

(**c**) 600 m above shallow gas formation

Figure 5. Settlement curves at different locations above shallow gas formation.

To further analyze the mechanism of formation settlement during the blowout process, the overall evolution laws of the geostress in the formation at different times were analyzed. Figure 7 presents the cloud diagram illustrating the variation of vertical effective stress in the formation over time. It reveals that, at the initial stage of the blowout, aside from the high-pressure shallow gas layer, the distribution of geostress in the remaining layers is relatively uniform, approximately equal to the dry weight of the formation. Following the escape of gas, under the influence of a higher pressure gradient, pressure within the shallow gas layer is released, resulting in an increase in vertical effective stress. This observation aligns with the principle of effective stress in soil mechanics. The earliest change occurs near the wellbore on the left side of the shallow gas layer. As time progresses, the area experiencing an increase in effective stress gradually expands, extending towards the right side of the shallow gas layer and both the upper and lower sides of the rock body. In contrast, regions far from the shallow gas layer are almost unaffected.
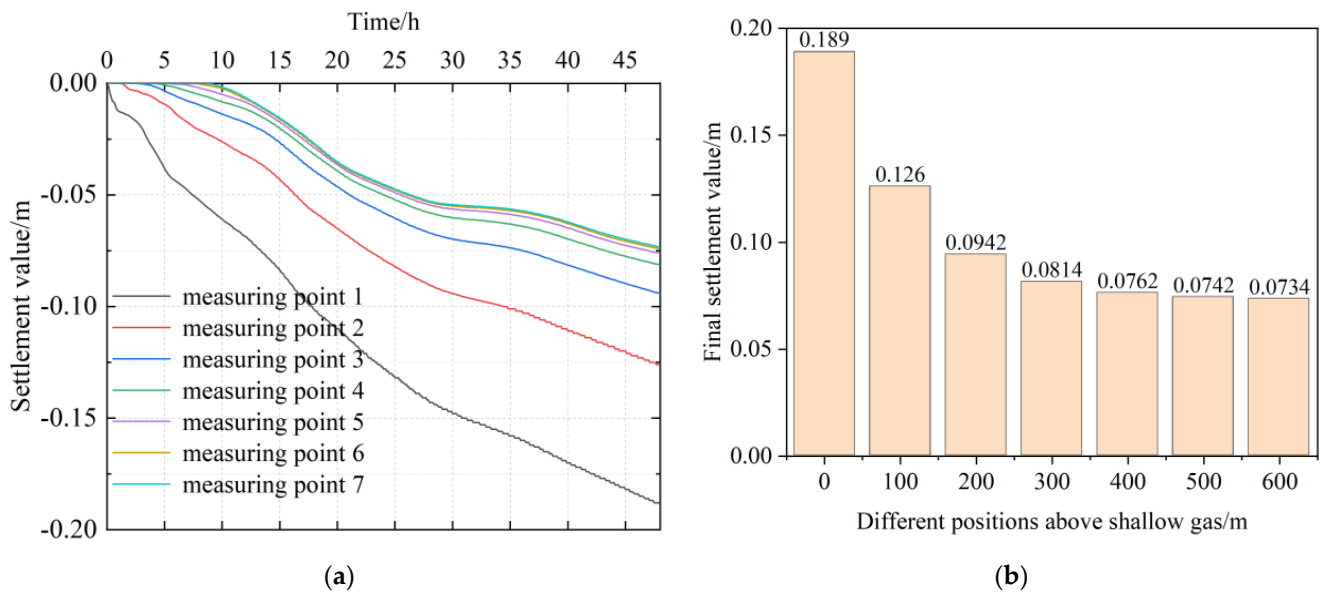
Figure 6. Wellbore settlement values (**a**) differenct positions (**b**) final sttlement values.
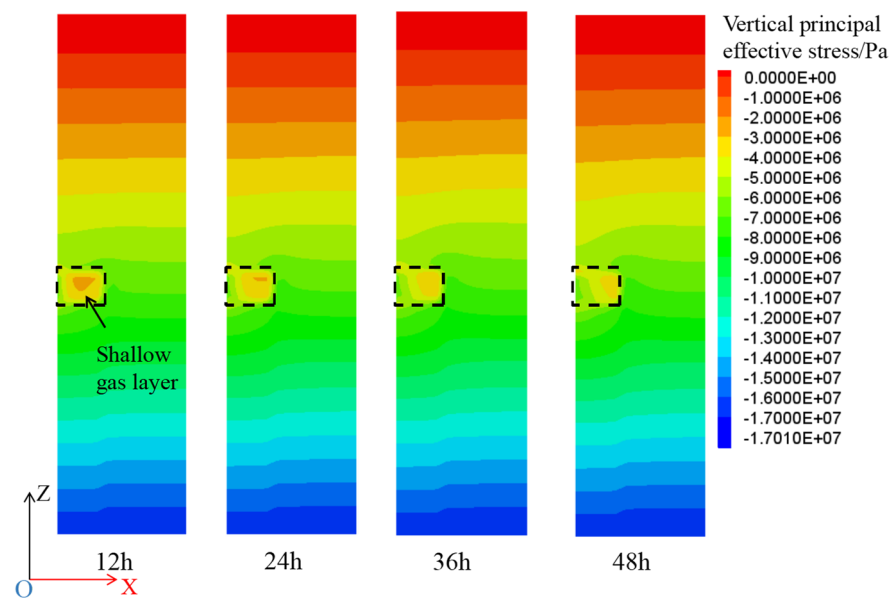
Figure 7. Cloud chart of vertical effective stress evolution during blowout process.

Figure 8 presents a cloud diagram depicting the variation in horizontal effective stress during the blowout process. As observed, similar to vertical effective principal stress, the horizontal effective principal stress within the shallow gas layer increases following the gas escape, with the area of increased stress continually expanding. Considering that not all the high-pressure gas within the shallow layer is expelled after 48 h, regions far from the wellbore within the shallow gas layer still exhibit high-pressure zones, where the effective principal stress is lower. The trend in the formation's effective stress changes indicates two primary reasons for significant deformation, especially in the shallow gas layer. Firstly, the extensive expulsion of mud and sand from the shallow gas layer increases the formation's porosity and weakens it considerably, leading to substantial deformation under the self-load of the rock. Secondly, the expulsion of a large amount of high-pressure gas from the shallow gas layer reduces the pore pressure, increasing the effective stress within the formation and further exacerbating its deformation.
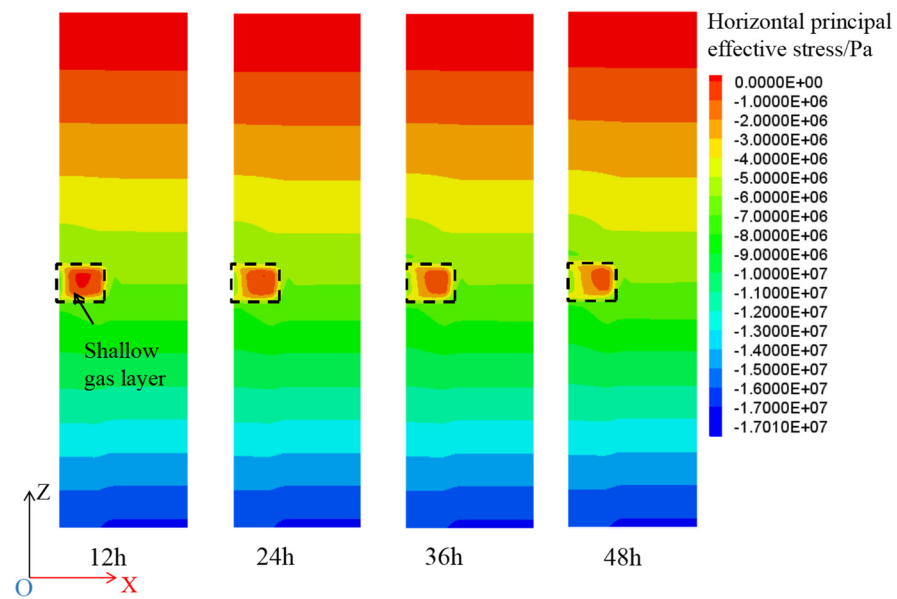
Figure 8. Cloud chart of horizontal effective stress evolution during blowout process.

A statistical analysis was conducted on the gas blowout rate and cumulative expelled gas volume from the shallow gas layer 48 h post blowout, with the results illustrated in Figure 9. It can be seen that the gas blowout rate initially exhibits a characteristic of a high initial rate followed by a rapid decline. The initial rate at the onset of the blowout nearly reaches 1.375×10^5 m^3/h, then gradually stabilizes to a rate of 3.70×10^4 m^3/h after 8 h. The cumulative volume of expelled gas progressively increases, although the rate of increase gradually diminishes. After two days, the cumulative expelled gas volume approaches nearly 2 million m^3. It is noteworthy that the focus of this paper is on the deformation characteristics of the formation following the expulsion of shallow gas. The recorded gas blowout volume refers to the flow rate at the bottom of the well, rather than the gas blowout volume at the wellhead.
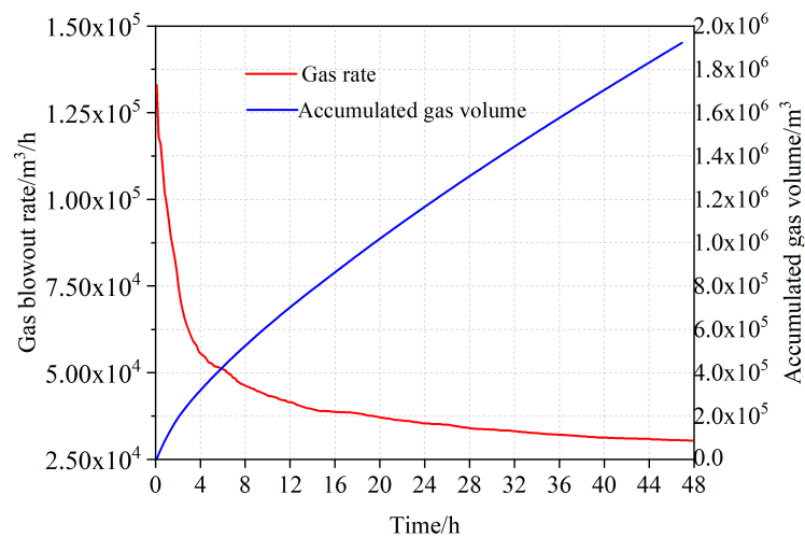
Figure 9. Variation curves of gas blowout rate and accumulated ejection volume during blowout process.

Figure 10 presents the sand blasting rate and the change in the quantity of sand during the blowout process. Similar to the gas blowout rate, the sand blasting rate exhibits a significant exponential decline over time. The initial sand blasting rate is relatively high, reaching 110 m^3/h. The cumulative sand blasting volume is positively correlated with time

and gradually stabilizes over two days. The main reason for this trend is attributed to the decrease in the gas blowout rate in the later stages of the blowout. This reduction lessens the erosion effect of the gas on the sand bodies in the shallow gas layer, thereby diminishing its sand-carrying capacity. The final cumulative amount of sand blasting volume over two days reaches 1600 m^3. This is close to the data monitored on site, which also proves the feasibility of our simulation.
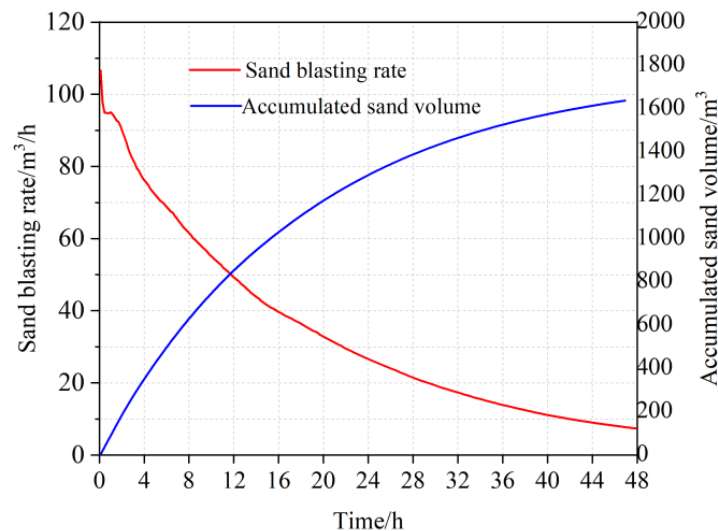

Figure 10. Variation curves of sand blasting rate and accumulated blasting volume during blowout process.

4.2. Sensitivity Analysis of Factors Affecting Geological Deformation

According to the simulation scheme provided in Table 2, the sensitivity analysis of factors was conducted. Considering the significant deformation observed at the top of the shallow gas layer and near the wellbore, which are potential areas for instability during a well blowout, the next study focuses on analyzing formation deformation along the measuring line (l_1) above the shallow gas layer.

(1) Burial depth.

Figure 11 presents the overall deformation cloud diagram of formations with different shallow gas burial depths 48 h after a blowout. It can be observed from the figure that the degree of formation deformation is positively correlated with the burial depth of the shallow gas layer. This is primarily because greater burial depths result in larger overburden loads from the overlying strata. After the ejection of mud and sand, the formation strength weakens. Under the effect of a larger overburden load, the amount of formation subsidence increases, making instability more likely. Although the settlement of shallow gas layers is relatively small when buried at a shallow depth, the upward range of settlement deformation is larger. Compared with models with larger burial depths, the seabed mudline is more affected by blowout.

Figure 12 shows the subsidence above the shallow gas layers of formations at different burial depths, and Figure 13 displays the maximum subsidence at various depths. It is evident from these figures that the maximum formation subsidence occurs above the shallow gas layer near the wellbore. The maximum settlement values in different burial depth models are 0.166 m, 0.193 m, 0.207 m, 0.220 m, and 0.229 m, respectively. It is noteworthy that the maximum subsidence increases with the depth of the shallow gas layer, but the rate of increase gradually diminishes. The primary reason for this is that when the pressure of the shallow gas layer remains constant, the pressure difference with the fluid column pressure inside the wellbore decreases as the burial depth increases. Consequently, the amount of sand ejection reduces, the degree of formation weakening

decreases, and although the overburden load increases, the shallow gas layer retains the capacity to withstand deformation.
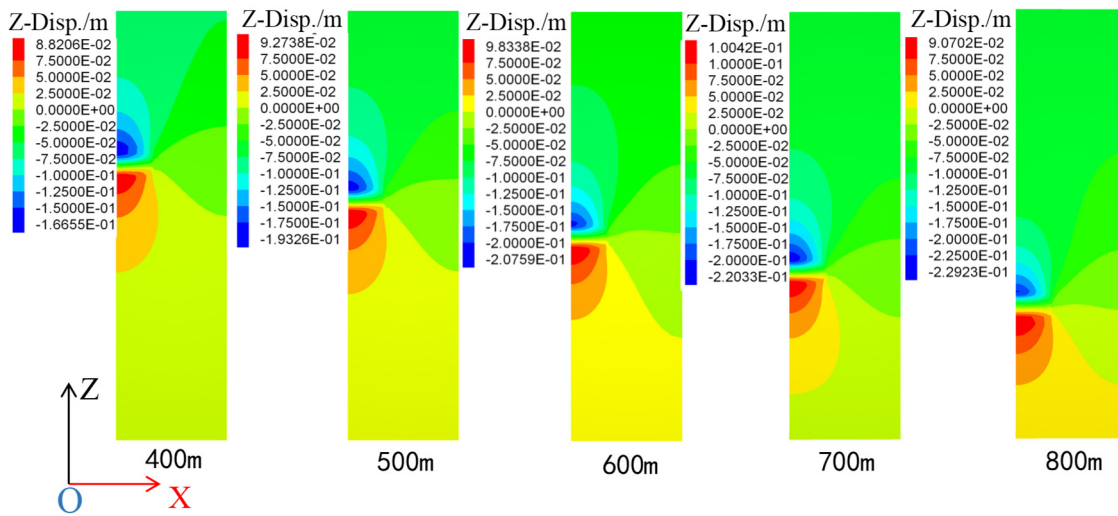

Figure 11. Overall deformation cloud maps under different shallow buried depths of gas layers 48 h after blowout.
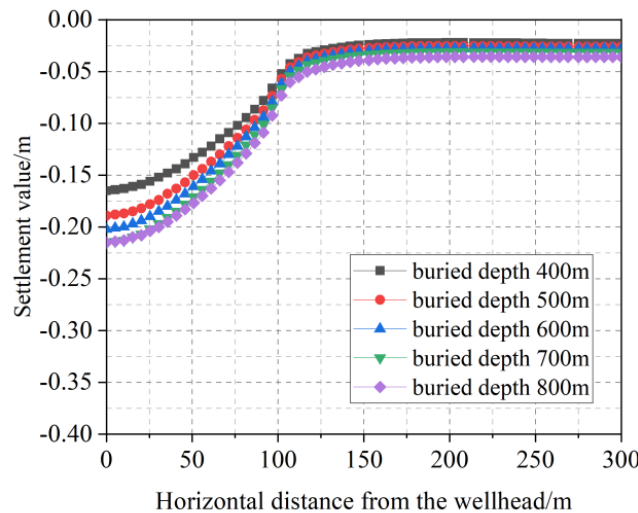

Figure 12. Subsidence curve of the stratum above the shallow gas layer under different buried depths of shallow gas.

(2)   Pressure coefficients.

Figure 14 presents the overall deformation cloud diagram of formations influenced by different shallow gas layer pressure coefficients 48 h after a well blowout. It can be seen from the figure that the degree of formation deformation is positively correlated with the pressure of the shallow gas layers. The settlement and floor heave increase with the increase in pressure, and the range of geological deformation gradually increases. The maximum settlement of different shallow gas pressure models is 0.008 m, 0.126 m, 0.207 m, 0.289 m, and 0.373 m, respectively. The maximum settlement shows a linear increasing trend with the increase in shallow gas pressure, and the growth rate is relatively stable. The primary reason for this is that with a constant bottom-hole pressure, the greater the pressure in the formation, the higher the gas ejection velocity due to the larger pressure difference, resulting in increased sand carryover and greater weakening of the shallow gas layers. Additionally, as the pressure of the shallow gas layers increases, the magnitude

of the maximum subsidence of the formation also progressively increases, indicating that variations in the pressure of the shallow gas layers significantly impact formation deformation (Figures 15 and 16).
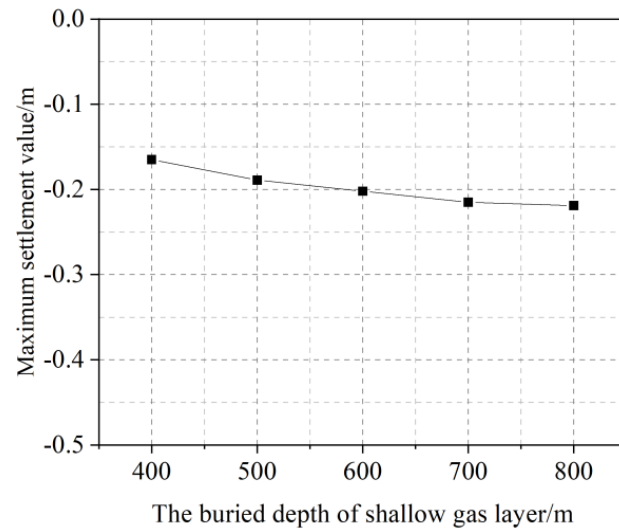

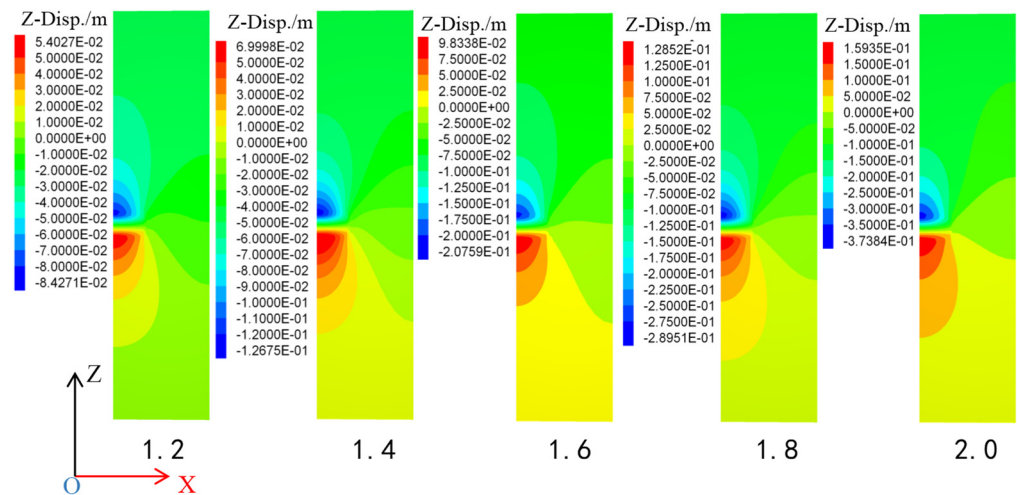**Figure 13.** The maximum settlement values under different buried depths of shallow gas.

Figure 14. Overall deformation cloud maps under different pressure coefficients 48 h after blowout.

(3)   Sand blasting volumes.

This study analyzed the degree of formation deformation for sand blasting volumes ranging from 300 m^3 to 1500 m^3. As evident from Figure 17, there is a positive correlation between the sand blasting volume and the overall deformation of the formation. The deformation amount and deformation range of the formation increase with the increase in sandblasting volume. The maximum settlement values in models with different sandblasting amounts are 0.002 m, 0.067 m, 0.102 m, 0.134 m, and 0.185 m, respectively. Compared with different gas pressure models, although the maximum settlement value also shows a linear increase trend, the increase rate is relatively low. In addition, when the sandblasting amount is small, the deformation amount of the formation in the early stage of the blowout is relatively small. The primary reason for this is that the ejection of a large quantity of mud and sand particles from the formation increases the porosity of the shallow gas layer, reduces the elastic modulus, and weakens the resistance to deformation. Under the influence of overburden load, the deformation of the formation increases. This significant deformation is mainly concentrated near the wellbore of the shallow gas layer,

with the maximum subsidence being almost directly proportional to the sand blasting volume, descending at a relatively uniform rate (Figures 18 and 19).
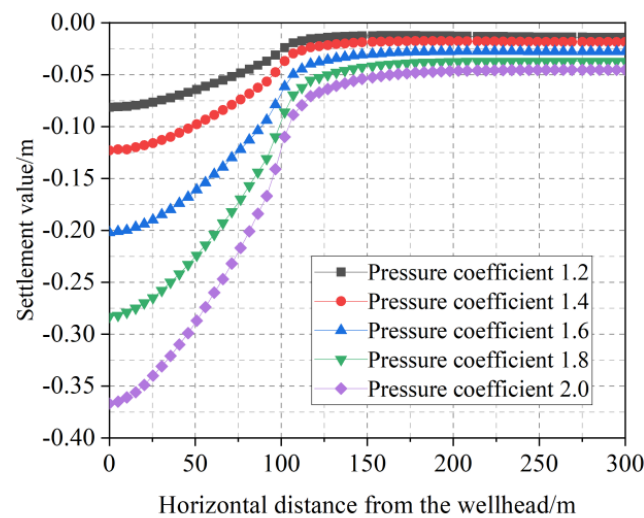

Figure 15. Subsidence curve of the stratum above the shallow gas layer under different pressure coefficients.
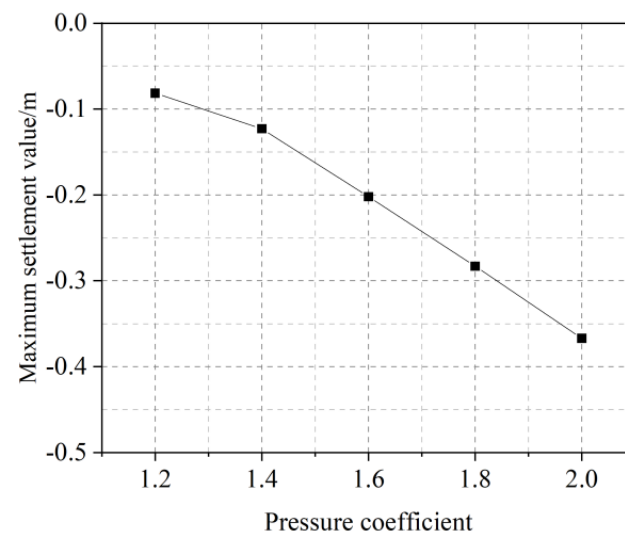

Figure 16. Maximum settlement values under different pressure coefficients.

(4)　Shallow gas layer range

Keeping the thickness of the shallow gas layer constant at 60 m, the range of the layer was controlled by adjusting its length, with lengths ranging from 60 m to 140 m analyzed. As shown in Figure 20, the degree of formation deformation across different ranges of the shallow gas layer is quite similar, with the maximum subsidence near the wellbore consistently around 0.2 m. The maximum settlement values in different models are 0.212 m, 0.213 m, 0.207 m, 0.207 m and 0.206 m, respectively, indicating that the shallow gas layer has a relatively small impact on the deformation at the bottom of the wellbore. This phenomenon is more apparent in Figures 21 and 22, where the subsidence curves for different shallow gas ranges at 60 m to the right of the wellbore almost coincide, and the slope of the maximum subsidence curve is nearly zero. This is primarily because the gas ejection speed near the wellbore is high, resulting in significant mud and sand loss and a high degree of formation weakening. Under the same pressure difference, the gas flow speed is similar across different ranges, leading to comparable degrees of deformation.
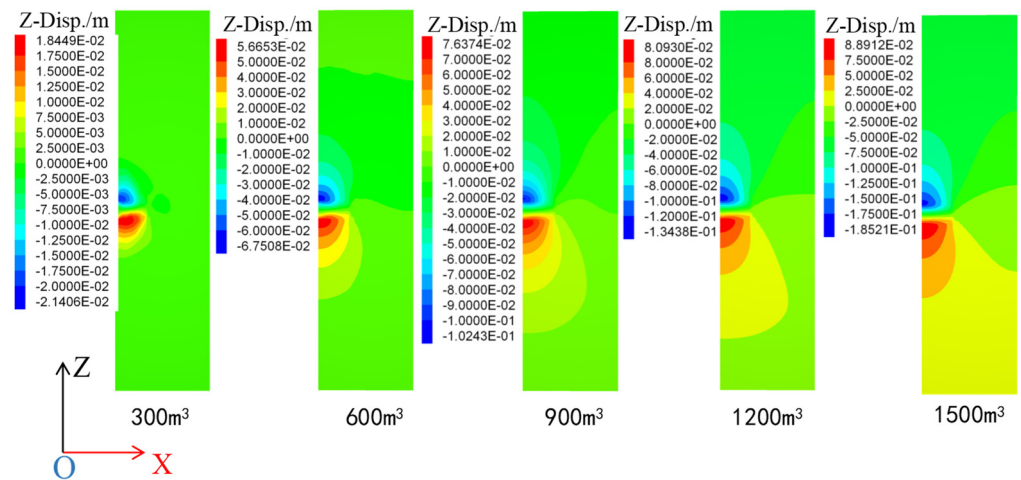
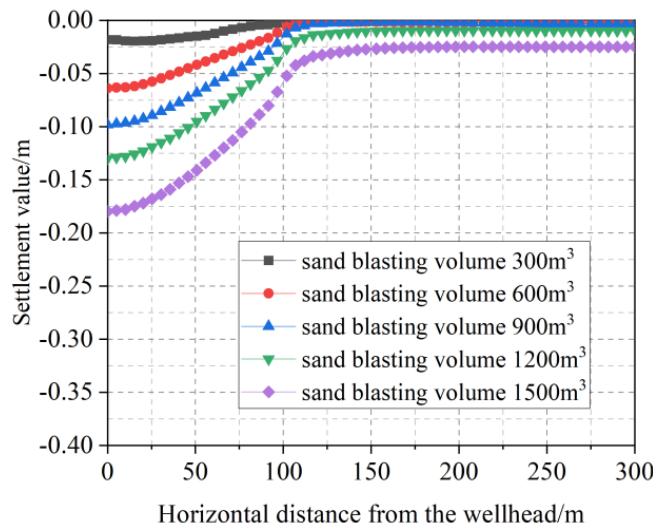**Figure 17.** Overall deformation cloud maps under different pressure sand blasting volumes 48 h after blowout.

Figure 18. Subsidence curve of the stratum above the shallow gas layer under different sand blasting volumes.
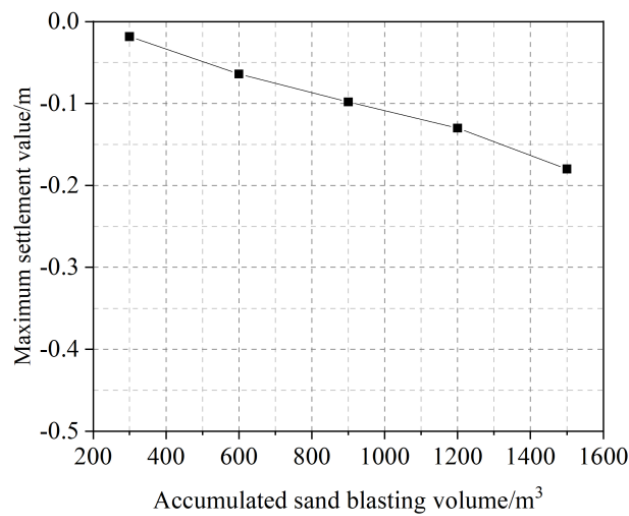

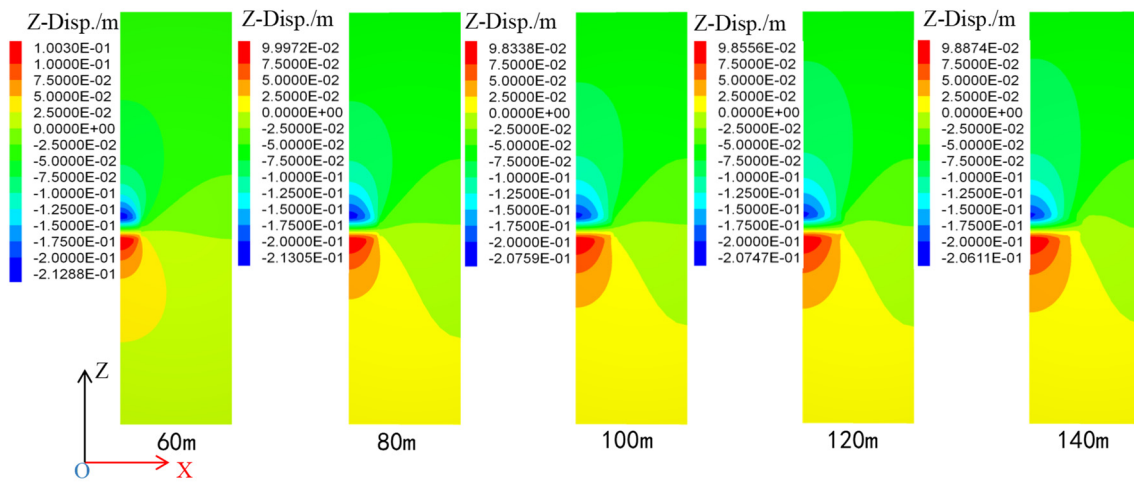**Figure 19.** Maximum settlement value under different sand blasting volumes.

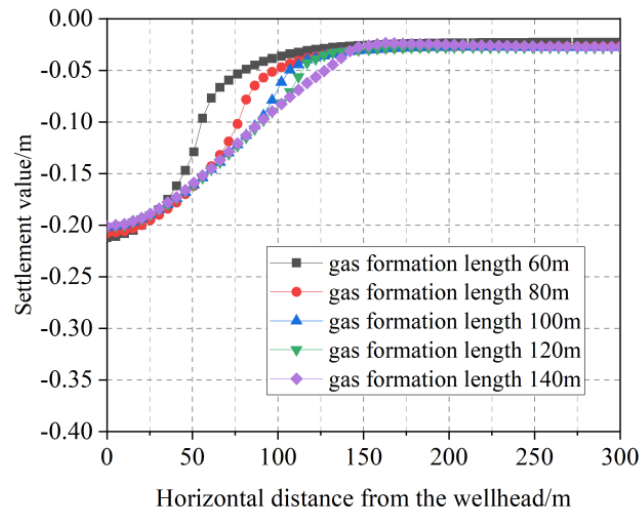**Figure 20.** Overall deformation cloud maps under different shallow gas layer ranges 48 h after blowout.

Figure 21. Subsidence curve of the stratum above the shallow gas layer under different shallow gas layer ranges.
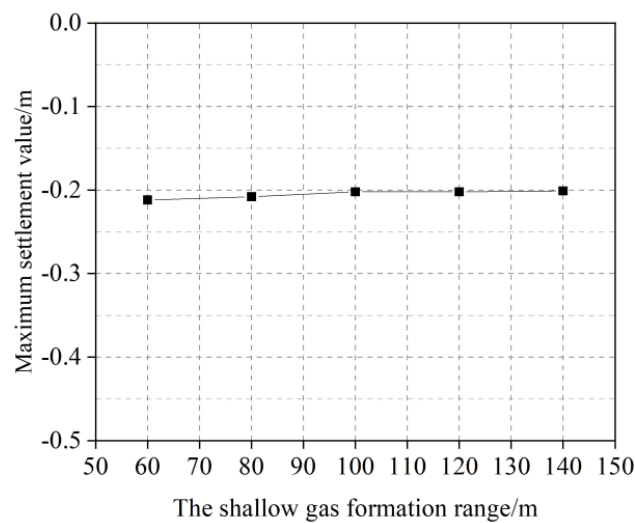
Figure 22. Maximum settlement value under different shallow gas layer ranges.

(5)   Gas blowout rate

Figure 23 presents the overall deformation cloud diagram of formations 48 h after a well blowout, influenced by different gas blowout rates. This figure shows that the overall deformation of the formation is positively correlated with the gas blowout rate. The maximum subsidence of strata in different models are 0.009 m, 0.210 m, 0.324 m, 0.354 m and 0.363 m respectively. As the gas blowout rate increases, both the subsidence and uplift of the formation increase. It is observed that the maximum subsidence near the wellbore increases with the gas blowout rate, but the rate of increase in subsidence gradually diminishes, eventually stabilizing at close to 0.36 m. The main reason for this is that at higher gas injection rates, the amount of sandblasting in shallow gas layers near the wellbore is similar, and the residual bearing capacity at that location gradually stabilizes. Under the same overlying load, the deformation of the formation also gradually becomes similar (Figures 24 and 25).
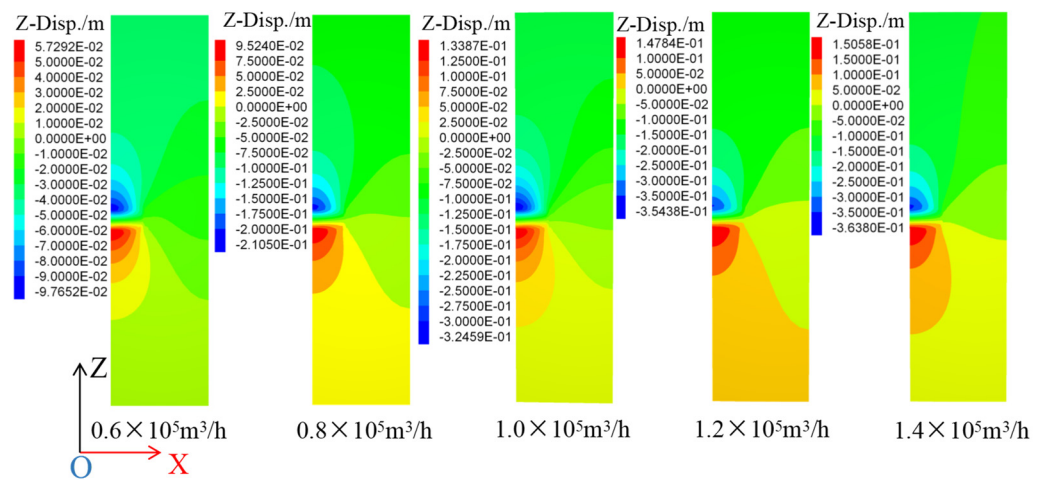

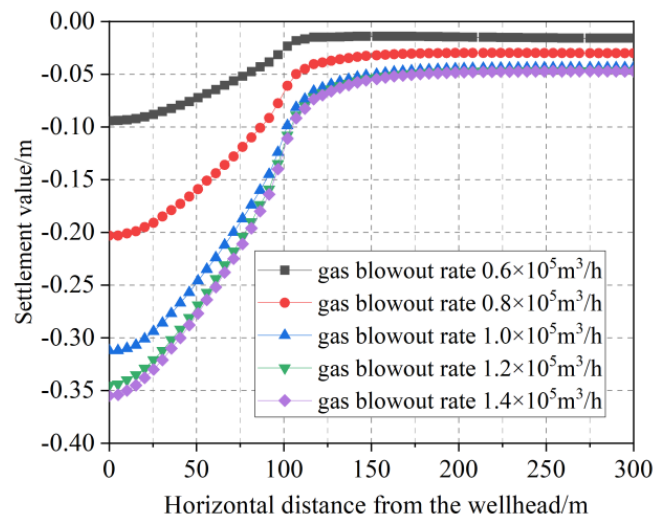**Figure 23.** Overall deformation cloud maps under different gas blowout rates 48 h after blowout.

Figure 24. Subsidence curve of the stratum above the shallow gas layer under different gas blowout rates.
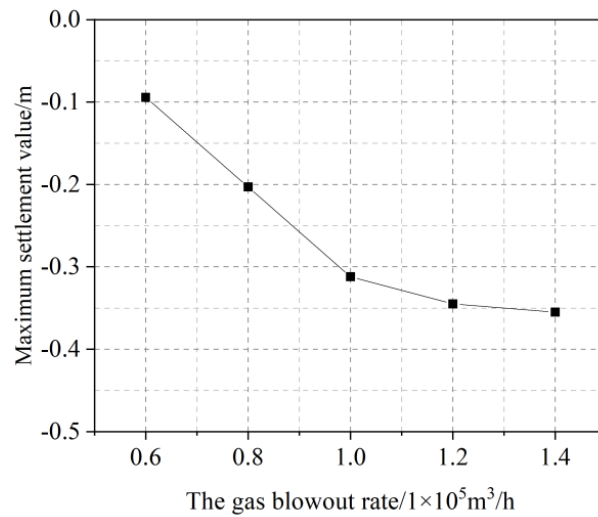
Figure 25. Maximum settlement value under different shallow gas blowout rates.

(6)   Pressure differences

When the formation pressure of the shallow gas layer is constant, pulling up the drill can create a suction pressure, reducing the overall pressure in the wellbore and disrupting the balance between bottom-hole pressure and formation pressure. The influence of five pressure differences of 1.26, 2.76, 4.26, 5.76, and 7.26 MPa on formation deformation were selected to analyze in this paper. As shown in Figure 26, the overall deformation of the formation is positively correlated with the pressure difference. Under the influence of a larger pressure gradient, the rate of gas blowout increases, carrying more sand and leading to greater weakening of the formation and increased deformation. The maximum settlement of models with different pressure differences are 0.113 m, 0.159 m, 0.207 m, 0.255 m, and 0.305 m, respectively (Figures 27 and 28).
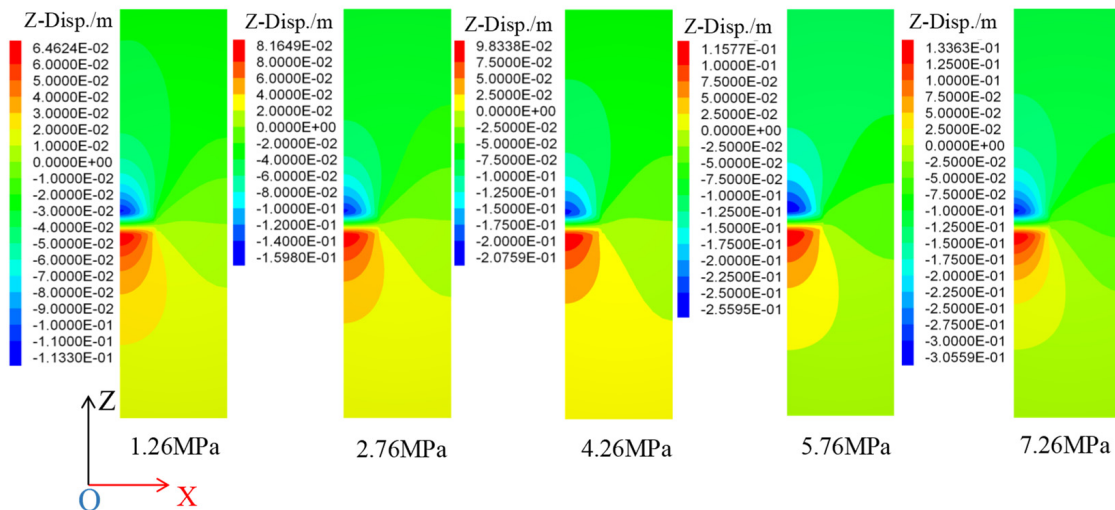

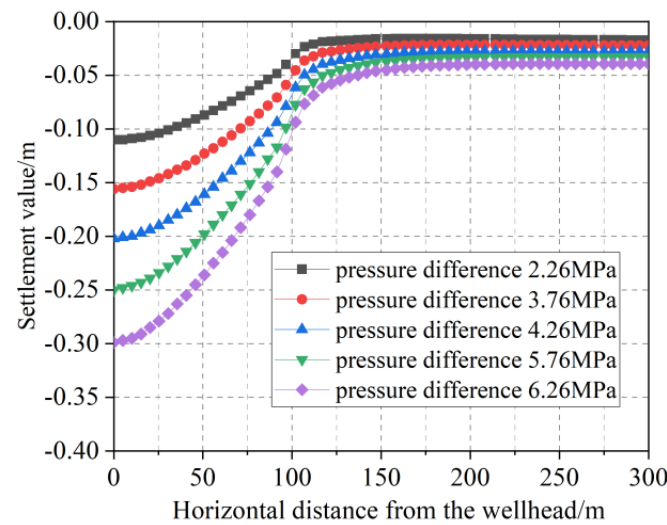**Figure 26.** Overall deformation cloud maps under different pressure differences 48 h after blowout.

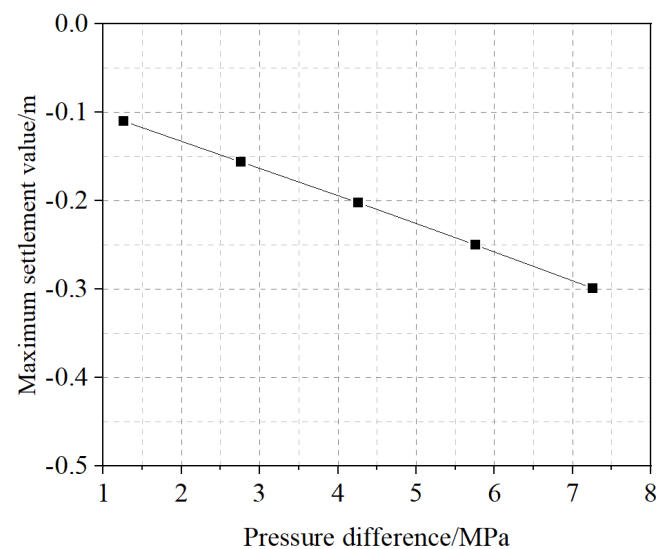**Figure 27.** Subsidence curve of the stratum above the shallow gas layer under different pressure differences.

Figure 28. Maximum settlement value under different pressure differences.

5. Conclusions

This paper, focusing on the formation deformation and instability disasters following shallow gas well blowouts, established a well blowout formation fluid–solid coupling theoretical model based on poroelastic theory combined with sand erosion criteria. It studied the spatiotemporal evolution of formation deformation post blowout and analyzed factors affecting the extent of formation deformation, yielding the following conclusions:

1. After a blowout, the shallow gas formation near the wellbore showed distinct subsidence and uplift, with deformation increasing over time. The maximum subsidence values at 12 h, 24 h, 36 h, and 48 h post blowout were 0.072 m, 0.132 m, 0.164 m, and 0.193 m, respectively, with a gradually decreasing rate.

2. Subsidence in the strata above the shallow gas layer formed a distinct "funnel" shape, with the maximum at the wellbore. Initially, the interlayer showed almost no deformation. Far-field formations were less affected by the blowout, exhibiting uniform subsidence, with the seabed mud line unaffected.

3. During the blowout, effective stress in the shallow gas layer and surrounding strata gradually increased, while regions far from the shallow gas layer remained almost unaffected. Both gas ejection and sand ejection rates initially decreased rapidly, then stabilized, following an exponential pattern.

4. Burial depth, pressure coefficient, sand blasting volume, shallow gas range, gas blowout rate, and bottom-hole pressure difference were all positively correlated with post-blowout formation deformation. Formation pressure, gas blasting rate, and bottom-hole pressure difference had a significant impact, followed by sand blasting volume and burial depth, while the range of the shallow gas layer had a weaker overall impact on formation deformation.

5. The numerical model in this paper was a two-dimensional model, concentrating solely on vertical formation deformation post blowout. Future work aims to develop a comprehensive three-dimensional thermal-hydraulic-mechanical coupling model. Additionally, the formation, simplified as a porous elastic body, had limitations. Future endeavors will explore plastic deformation and failure characteristics following blowouts.

Author Contributions: Conceptualization, Supervision, Z.Y., Z.H. and Y.M.; Software, Investigation, Formal analysis, X.Y. (Xiangqian Yang), X.Y. (Xinjiang Yan) and P.Z.; Writing—Original Draft, Y.L.; Writing—Review and Editing, Z.H. and Z.Y.; funding acquisition, Z.Y. and Y.M. All authors have read and agreed to the published version of the manuscript.

Data Availability Statement: Data is contained within the article.

References

1. Yan, C.; Li, Y.; Cheng, Y.; Wei, J.; Tian, W.; Li, S.; Wang, Z. Multifield coupling mechanism in formations around a wellbore during the exploitation of methane hydrate with CO_2 replacement. *Energy* **2022**, *245*, 123283. [CrossRef]
2. Wang, Q.; Lü, Y.; Li, Q. A review on submarine oil and gas leakage in near field: Droplets and plume. *Environ. Sci. Pollut. Res.* **2022**, *29*, 8012–8025. [CrossRef]
3. Seyyedattar, M.; Zendehboudi, S.; Butt, S. Invited review—Molecular dynamics simulations in reservoir analysis of offshore petroleum reserves: A systematic review of theory and applications. *Earth-Sci. Rev.* **2019**, *192*, 194–213. [CrossRef]
4. Brkić, D.; Stajić, Z. Offshore Oil and Gas Safety: Protection against Explosions. *J. Mar. Sci. Eng.* **2021**, *9*, 331. [CrossRef]
5. Farahani, M.V.; Hassanpouryouzband, A.; Yang, J.H.; Tohidi, B. Insights into the climate-driven evolution of gas hydrate-bearing permafrost sediments: Implications for prediction of environmental impacts and security of energy in cold regions. *RSC Adv.* **2021**, *11*, 14334–14346. [CrossRef]
6. Li, Q.; Zhang, C.; Yang, Y.; Ansari, U.; Han, Y.; Li, X.; Cheng, Y. Preliminary experimental investigation on long-term fracture conductivity for evaluating the feasibility and efficiency of fracturing operation in offshore hydrate-bearing sediments. *Ocean Eng.* **2023**, *281*, 114949. [CrossRef]
7. Farahani, M.V.; Hassanpouryouzband, A.; Yang, J.; Tohidi, B. Development of a coupled geophysical–geothermal scheme for quantification of hydrates in gas hydrate-bearing permafrost sediments. *Phys. Chem. Chem. Phys.* **2021**, *23*, 24249–24264. [CrossRef] [PubMed]
8. Yan, C.; Ren, X.; Cheng, Y.; Song, B.; Li, Y.; Tian, W. Geomechanical issues in the exploitation of natural gas hydrate. *Gondwana Res.* **2020**, *81*, 403–422. [CrossRef]
9. Choi, J.; Kang, N.-K.; Hwang, I.G.; Lee, D.-H. Geochemical characteristics and origins of hydrocarbon gases in the shallow gas field in the Pohang Basin, Korea. *Geosci. J.* **2022**, *26*, 349–365. [CrossRef]
10. Müller, S.; Reinhardt, L.; Franke, D.; Gaedicke, C.; Winsemann, J. Shallow gas accumulations in the German North Sea. *Mar. Pet. Geol.* **2018**, *91*, 139–151. [CrossRef]
11. Sun, Q.; Wu, S.; Cartwright, J.; Dong, D. Shallow gas and focused fluid flow systems in the Pearl River Mouth Basin, northern South China Sea. *Mar. Geol.* **2012**, *315*, 1–14. [CrossRef]
12. Seyyedattar, M.; Zendehboudi, S.; Butt, S. Technical and Non-technical Challenges of Development of Offshore Petroleum Reservoirs: Characterization and Production. *Nat. Resour. Res.* **2020**, *29*, 2147–2189. [CrossRef]
13. Xue, L.; Fan, J.; Rausand, M.; Zhang, L. A safety barrier-based accident model for offshore drilling blowouts. *J. Loss Prev. Process Ind.* **2013**, *26*, 164–171. [CrossRef]

14. Yin, B.; Li, B.; Liu, G.; Wang, Z.; Sun, B. Quantitative risk analysis of offshore well blowout using bayesian network. *Saf. Sci.* **2021**, *135*, 105080. [CrossRef]
15. Li, X.; Abbassi, R.; Chen, G.; Wang, Q. Modeling and analysis of flammable gas dispersion and deflagration from offshore platform blowout. *Ocean Eng.* **2020**, *201*, 107146. [CrossRef]
16. Khakzad, N.; Khakzad, S.; Khan, F. Probabilistic risk assessment of major accidents: Application to offshore blowouts in the Gulf of Mexico. *Nat. Hazards* **2014**, *74*, 1759–1771. [CrossRef]
17. Zhu, J.; Chen, G.; Yin, Z.; Khan, F.; Meng, X. An integrated methodology for dynamic risk evaluation of deepwater blowouts. *J. Loss Prev. Process Ind.* **2022**, *74*, 104647. [CrossRef]
18. Yang, D.; Chen, G.; Shi, J.; Li, X. Effect of gas composition on dispersion characteristics of blowout gas on offshore platform. *Int. J. Nav. Arch. Ocean Eng.* **2019**, *11*, 914–922. [CrossRef]
19. Socolofsky, S.A.; Jun, I.; Boufadel, M.C.; Liu, R.; Lu, Y.; Arey, J.S.; McFarlin, K.M. Development of an offshore response guidance tool for determining the impact of SSDI on released gas and benzene from artificial subsea oil well blowout simulations. *Mar. Pollut. Bull.* **2022**, *184*, 114114. [CrossRef] [PubMed]
20. Tamim, N.; Laboureur, D.M.; Mentzer, R.A.; Hasan, A.R.; Mannan, M.S. A framework for developing leading indicators for offshore drillwell blowout incidents. *Process Saf. Environ. Prot.* **2017**, *106*, 256–262. [CrossRef]
21. Jiao, Z.R.; Yuan, S.; Ji, C.X.; Mannan, M.S.; Wang, Q.S. Optimization of dilution ventilation layout design in confined environ-ments using Computational Fluid Dynamics (CFD). *J. Loss Prev. Process. Ind.* **2019**, *60*, 195–202. [CrossRef]
22. Yi, H.; Feng, Y.; Wang, Q. Computational fluid dynamics (CFD) study of heat radiation from large liquefied petroleum gas (LPG) pool fires. *J. Loss Prev. Process Ind.* **2019**, *61*, 262–274. [CrossRef]
23. Wang, J.; Wang, M.; Yu, X.; Zong, R.; Lu, S. Experimental and numerical study of the fire behavior of a tank with oil leaking and burning. *Process Saf. Environ. Prot.* **2022**, *159*, 1203–1214. [CrossRef]
24. Tan, W.; Wang, K.; Li, C.; Liu, L.; Wang, Y.; Zhu, G. Experimental and numerical study on the dispersion of heavy gases in urban environments. *Process Saf. Environ. Prot.* **2018**, *116*, 640–653. [CrossRef]
25. Zhang, L.; Wu, S.; Zheng, W.; Fan, J. A dynamic and quantitative risk assessment method with uncertainties for offshore managed pressure drilling phases. *Saf. Sci.* **2018**, *104*, 39–54. [CrossRef]
26. Guo, Y.; Sun, B.; Gao, Y.; Li, H.; Wu, C. Gas kick during carbonate reservoirs drilling and its risk assessment. *Pet. Explor. Dev.* **2017**, *44*, 462–469. [CrossRef]
27. Sun, Z.-Y.; Zhou, J.-L.; Gan, L.-F. Safety assessment in oil drilling work system based on empirical study and Analytic Network Process. *Saf. Sci.* **2018**, *105*, 86–97. [CrossRef]
28. Meng, H.; An, X. Dynamic risk analysis of emergency operations in deepwater blowout accidents. *Ocean Eng.* **2021**, *240*, 109928. [CrossRef]
29. Dadashzadeh, M.; Ahmad, A.; Khan, F. Dispersion modelling and analysis of hydrogen fuel gas released in an enclosed area: A CFD-based approach. *Fuel* **2016**, *184*, 192–201. [CrossRef]
30. Ma, Q.C.; Zhang, L.B. CFD simulation study on gas dispersion for risk assessment: A case study of sour gas well blowout. *Saf. Sci.* **2011**, *49*, 1289–1295.
31. Li, X.; Chen, G.; Zhu, H.; Xu, C. Gas dispersion and deflagration above sea from subsea release and its impact on offshore platform. *Ocean Eng.* **2018**, *163*, 157–168. [CrossRef]
32. Li, X.; Chen, G.; Zhang, R.; Zhu, H.; Xu, C. Simulation and assessment of gas dispersion above sea from a subsea release: A CFD-based approach. *Int. J. Nav. Arch. Ocean Eng.* **2019**, *11*, 353–363. [CrossRef]
33. Lei, Y.; Sun, J.; Wang, G. Simulation of Shallow Gas Invasion Process During Deepwater Drilling and Its Control Measures. *J. Ocean Univ. China* **2022**, *21*, 707–718. [CrossRef]
34. Cheng, K.; Wang, Y.; Yang, Q. A semi-resolved CFD-DEM model for seepage-induced fine particle migration in gap-graded soils. *Comput. Geotech.* **2018**, *100*, 30–51. [CrossRef]
35. Papamichos, E.; Vardoulakis, I.; Tronvoll, J.; Skjærstein, A. Volumetric sand production model and experiment. *Int. J. Numer. Anal. Methods Geomech.* **2010**, *25*, 789–808. [CrossRef]
36. Papamichos, E.; Vardoulakis, I. Sand erosion with a porosity diffusion law. *Comput. Geotech.* **2005**, *32*, 47–58. [CrossRef]
37. Latief, F.D.E.; Fauzi, U. Kozeny–Carman and empirical formula for the permeability of computer rock models. *Int. J. Rock Mech. Min. Sci.* **2012**, *50*, 117–123. [CrossRef]
38. Liang, Y.; Cheng, Y.; Han, Z.; Pidho, J.J.; Yan, C. Study on Multiscale Fluid–Solid Coupling Theoretical Model and Productivity Analysis of Horizontal Well in Shale Gas Reservoirs. *Energy Fuels* **2023**, *37*, 5059–5077. [CrossRef]
39. Wei, W.; Cai, J.; Xiao, J.; Meng, Q.; Xiao, B.; Han, Q. Kozeny-Carman constant of porous media: Insights from fractal-capillary imbibition theory. *Fuel* **2018**, *234*, 1373–1379. [CrossRef]